

Noble gas evidence of a millennial-scale deep North Pacific palaeo-barometric anomaly

Received: 9 July 2022

W. J. Jenkins¹✉, A. M. Seltzer¹, G. Gebbie² & C. R. German³

Accepted: 20 December 2023

Published online: 24 January 2024

 Check for updates

Precise measurements of dissolved noble gases along the GP15 GEOTRACES Pacific Meridional Transect reveal the oldest northern bottom waters equilibrated with the atmosphere at a higher barometric pressure than more recent waters. Here, using a radiocarbon-calibrated multi-tracer-based diagnostic model, we reconstruct the magnitude and timing of this palaeo-barometric pressure anomaly. We hypothesize this multi-millennial trend in sea-level pressure results from local and regional processes extant in Antarctic Bottom Water formation regions.

Being inert, noble gases usefully trace water mass formation processes. Excluding the lightest (helium) and heaviest (radon), they have no internal sources or sinks within the ocean and therefore preserve a record of conditions when water masses leave the ocean surface¹ in polar regions. These gases (Ne, Ar, Kr and Xe) have a wide range of well-determined physical characteristics, including solubility² and molecular diffusivity³. Processes at these interfaces imprint the concentrations of the individual noble gases in unique ways^{1,4,5}, and the patterns are preserved over the trajectory of the water masses as they circumnavigate the global meridional overturning circulation (MOC⁶), subject only to mixing and advection. The deep Pacific records the oldest climate events because it is the terminus of the MOC.

Gases are generally super- or undersaturated in subsurface waters, where ΔC , the ‘saturation anomaly’, is defined as the per cent deviation from solubility equilibrium with the atmosphere:

$$\Delta C = \left(\frac{C}{C_s} - 1 \right) \times 100\%. \quad (1)$$

C is the measured concentration and C_s is the saturation concentration of the gas at the water’s temperature and salinity when in contact at a reference pressure of precisely 1,013.25 mbar (ref. 2). Sea-level pressure (SLP) is rarely exactly equal to this reference value, because it is affected by local and large-scale meteorological processes. Moreover, processes at the sea surface, including wind-induced bubble injection and radiative heating and cooling, drive gases away from equilibrium. Within the deep Pacific Ocean, noble gases exhibit a consistent pattern where the lightest noble gas (Ne) is slightly supersaturated and the heavier gases (Ar, Kr and Xe) are progressively more undersaturated,

resulting from their differing physical characteristics in response to these competing processes during water mass formation^{4,7}.

In this Brief Communication, as part of the US GEOTRACES programme, we measured dissolved noble gases along a meridional section (GP15) in the central Pacific (–152° W) from 20.0° S to 56.5° N. We analysed –850 samples from 36 locations along this track⁸ at an analytical precision of order 0.1% (see refs. 2,7). Figure 1a is a contoured section of dissolved neon concentrations, showing a pronounced maximum in bottom waters north of 10° N. This feature appears in the contoured neon saturation anomaly ΔNe (Fig. 1b). Figure 1b is overlaid with an idealized schematic of the deep MOC depicted in ref. 9, which has bottom water entering from the south below –3,400 m depth, upwelling in the North Pacific and returning below –2,000 m depth towards the south. All of the noble gases are influenced by incoming bottom water⁸. Although the ΔNe maximum appears to extend the full depth of the water column, careful inspection reveals a clear separation between shallower and deeper features around the –2,200 m depth, which coincides with the upper extent of the overturning circulation scheme⁸. We focus on the lower feature.

Average saturation anomalies of all four noble gases below the 28.05 kg m^{–3} neutral density surface, binned in 10°-latitude increments, exhibit a consistent northward increase (Extended Data Fig. 1). Comparison of averages between the northern (25° to 45° N) and southern (20° S to 0° N) bottom waters, corrected for the influence of geothermal heating, reveals a net increase of $0.30 \pm 0.05\%$, $0.26 \pm 0.05\%$, $0.31 \pm 0.12\%$ and $0.22 \pm 0.08\%$ for ΔNe , ΔAr , ΔKr and ΔXe , respectively. Although small in magnitude, these differences are well resolved due to both high analytical precision² and the number of samples measured in the northern ($n = 25$) and southern ($n = 35$) group for each gas.

¹Department of Marine Chemistry and Geochemistry, Woods Hole Oceanographic Institution, Woods Hole, MA, USA. ²Department of Physical Oceanography, Woods Hole Oceanographic Institution, Woods Hole, MA, USA. ³Department of Geology and Geophysics, Woods Hole Oceanographic Institution, Woods Hole, MA, USA. ✉e-mail: wjenkins@whoi.edu

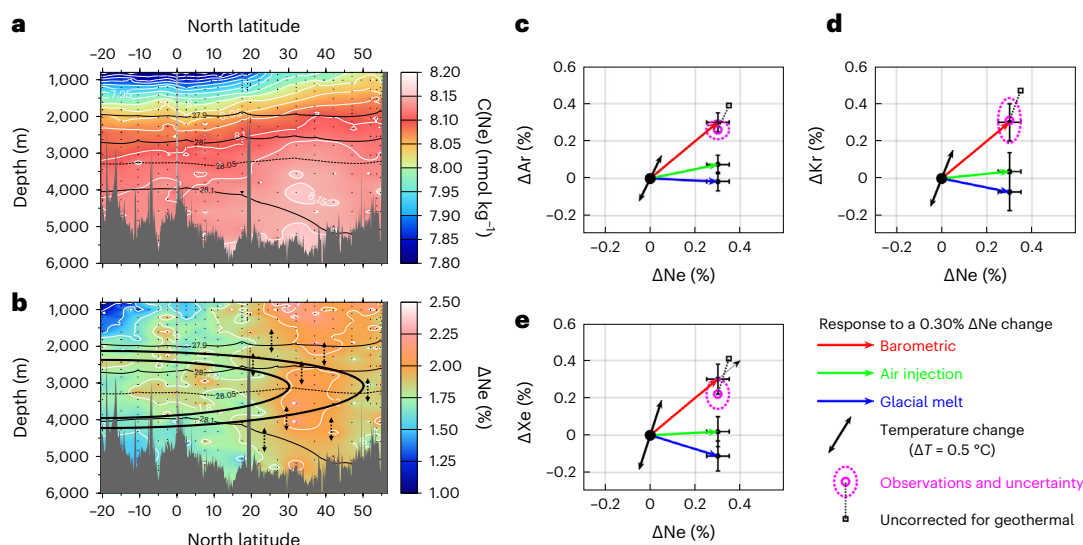


Fig. 1 | Noble gas variations in the deep Pacific. **a**, A contoured S–N section (depth versus latitude) of dissolved neon concentration (in nmol kg^{-1}) in the central Pacific along -152° W from 20° S to Alaska. The sea floor is dark grey, and black dots represent sample locations. White contours are concentration isopleths (contour interval -2σ). The thin black contours are the neutral density anomaly, where the 28.05 kg m^{-3} marks the boundary between incoming bottom water and returning deep water. **b**, The same data expressed as saturation anomaly (ΔNe in %, see equation (1) in text). Superimposed on the section (heavier black lines) is a schematic of overturning streamlines for this section recently proposed by Holzer et al. (adapted from their Fig. 1b⁹). The black vertical dashed arrows schematically depict vertical mixing. Note there is a mid-depth vertical minimum in ΔNe around 2,300 m in the north separating the deep and intermediate waters. **c–e**, Schematic noble gas saturation anomaly changes

corresponding to a ΔNe increase of 0.30% between the northern and southern regions in Ar (**c**), Kr (**d**) and Xe (**e**) after a correction for geothermal heating of 0.05°C (original, uncorrected data are small black squares; the corrected data are the magenta circles with surrounding error ellipses). The black error bars indicate the approximate uncertainty (one s.d.) in the projections, while the different coloured vectors indicate the changes due to the four candidate processes considered here. The upward black vector indicates the saturation anomaly change due to geothermal heating of 0.05°C , while the downward black vector signifies the thermal (cooling) disequilibrium of the same magnitude. The magenta ellipse signifies the uncertainty (1 s.e.m.) in the differences between mean northern ($n = 35$) and southern ($n = 25$) bottom water noble gas saturation anomalies.

Systematic uncertainties are avoided by employing the same analytical procedures, standards and instruments used to determine their respective solubilities².

Since there are no in situ sources or sinks for these gases, we must conclude that the observed differences reflect past changes in water mass formation conditions. These can be decomposed into four possible mechanisms (the coloured arrows in Fig. 1c–e): changing mean wind speed (varying the amount of bubble injection¹, green arrows), variation in thermal disequilibrium (black arrows), changing glacial melt water addition (blue arrows) and altered atmospheric pressure (red arrows). Given that the response of the individual noble gases to each of these processes is unique and predictable¹⁰, the diagrams show that only changing barometric pressure can consistently explain the meridional differences in the four gases. The mean difference for all four gases of $0.28 \pm 0.04\%$ corresponds to a barometric pressure difference of $2.8 \pm 0.4 \text{ mbar}$ between the older bottom waters in the North Pacific and the younger bottom waters to the south.

This record of the original change must have been attenuated by subsequent mixing of different-aged water masses as they travel along the MOC. We use a radiocarbon-calibrated global ocean diagnostic model to account for this mixing and establish timing^{11,12}. We arbitrarily divide the past record into six 500-year ‘epochs’ that roughly correspond to major climatic events (Extended Data Table 1). These choices are purely illustrative since the model integration is effectively continuous.

As expected^{6,9}, the northeast Pacific pools the older vintages (Extended Data Fig. 2), for example, the Roman Warm Period (RWP) and the Dark Ages Cold Period (DACP), whereas the South Pacific is dominated by the Medieval Climate Anomaly (MCA) and the Little Ice Age (LIA). The patterns also reflect the detailed bottom water circulation and the impact of mixing on their large-scale distributions.

Each averaging region contains a blend of vintages in proportions that vary with location. This is seen in more detail in Fig. 2a, which shows the percentage bottom water vintages along our section. MCA remains the dominant vintage along the section, while the LIA decreases northward. The older vintages (DACP, RWP and pre-RWP) gradually increase into the North Pacific, each approaching or exceeding the percentage of LIA north of 20° N. The modern vintage (MOD) is inconsequentially small. Using the same depth and latitude criteria that we employed to compute the noble gas averages, we estimate the average vintage mixtures for the southern and northern ‘endmembers’.

Because the problem is underdetermined, we perform an inverse calculation to solve for the mean epoch SLP anomalies (SLPa) and their uncertainties (Fig. 2b) that minimizes the overall SLP trend and inter-epoch variance (Methods, Extended Data Figs. 3 and 4 and Extended Data Table 2). Entanglement of so many vintages means that we cannot realistically determine the absolute SLPa of each ‘epoch’, and the calculation smooths out variations on shorter timescales, which are masked by the error (Extended Data Fig. 4). Moreover, the SLPa is expressed relative to the average SLP of all vintages excluding MOD and remains untethered to the present day, whose vintage representation in the two regions is too low. The long-term SLPa trend, however, is robust and depicts a clear SLP contrast between the RWP and LIA. Hence, the complementary trends of increasing older vintages and decreasing younger vintages as one goes from south to north means that the observed palaeo-barometric gradient must arise from a long-term decreasing trend in SLP above the formation regions of $16 \pm 6 \text{ mbar}$ over two millennia. The observed (2.8 mbar) noble gas signal requires a larger SLP change in the past because of the damping effects of mixing between different aged waters. The error bars (Fig. 2b and Extended Data Table 1) account for the sensitivity of this reconstruction to the input data and its uncertainty.

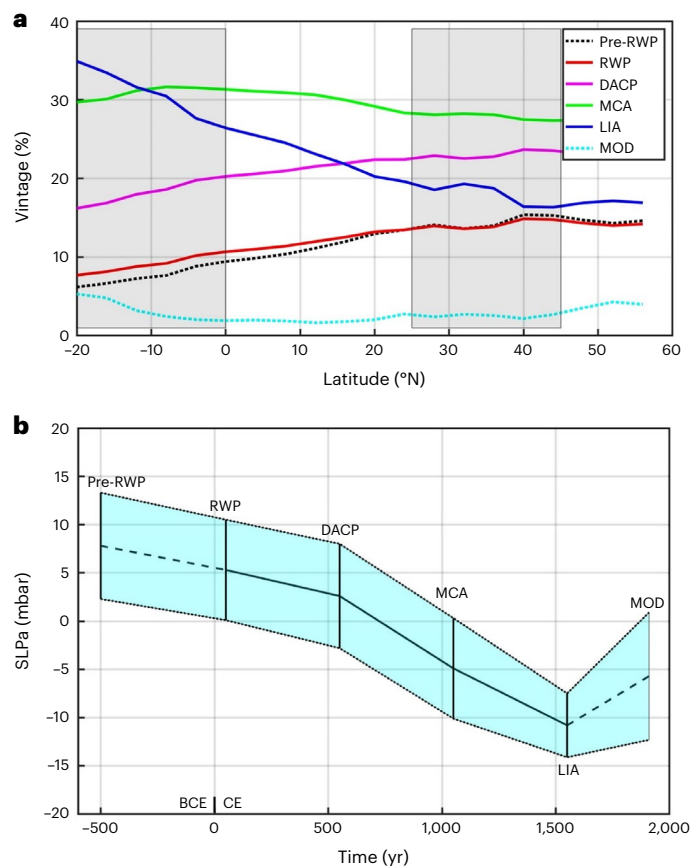


Fig. 2 | Model-estimated epoch mixtures and sea-level pressures for Pacific Bottom Waters. **a**, The relative amounts of model bottom water (below 3,400 m depth) vintages along the section. Regional averages are indicated as grey areas. See Methods for actual time period definitions. **b**, The approximately 2,000-year trend in SLPa and its uncertainty (shading) inferred from the radiocarbon constrained TMI calculation by Gebbie and Huybers¹². The uncertainties are ± 1 s.d. of the model's most probable values. The solution is based on the observed palaeo-barometric difference of 2.8 mbar in the bottom water between the two regions and subject to the joint constraints of minimizing long-term trend and variance. The vertical lines represent the range of possible values of SLPa at the centre point of each epoch. Note that the centre point of the pre-RWP period is arbitrary and uncertain. Since the percentages are so low for the modern vintage (MOD) in the regions considered in this study (Fig. 2a), the SLPa is referenced to the average SLP of all vintages except the MOD. As a result, the record remains essentially only weakly tethered to modern values. Furthermore, the solution will miss substantial unresolved decade-to-century variations within and between epochs inside the shaded uncertainty limits. Nevertheless, the overall trend of 16 ± 6 (1 s.d.) mbar between the RWP and LIA is robust.

The chronology depicted in Fig. 2b has substantial uncertainty, largely due to the fact that we are using a steady-state model of a system that is undoubtedly changing in time. Although it is difficult to assign a precise uncertainty, we contend this may be of order 20–30% (Methods). However, this does not invalidate the basic sense of the changes we depict in Fig. 2b. A prognostic, climate-responsive model will eventually be required for interpreting these observations.

The dominant fraction of bottom water in the Pacific originates from the regions around the Antarctic Continent¹³, so the observed gradients must result largely from past changes in SLP in the water mass formation regions around Antarctica. The SLP over these regions is strongly influenced by conditions and processes associated with bottom water formation itself, which occurs predominantly in coastal polynyas^{14,15} created by katabatic winds descending from the glaciated continent that drive forming sea ice away from the coast¹⁶. These semi-permanent features exert a profound regional influence on

local SLP patterns because of the large atmospheric buoyancy fluxes associated with interaction between the extremely cold katabatic winds and the warm exposed surface ocean water¹⁶. When large enough, polynyas can generate mesoscale cyclones with local SLPa ranging from approximately -10 to -20 mbar^{17,18}. Hence, the frequency, size and extent of polynya formation, driven by the intensity of katabatic winds, and ultimately regional temperatures and atmospheric pressure fields, probably modulate the effective SLP that sets Antarctic Bottom Water (AABW) dissolved gas contents.

The substantial negative SLP excursion inferred here during the LIA is not consistent with proxy records of the Southern Annular Mode index¹⁹. Instead, evidence of colder Antarctic climatic conditions²⁰ during the LIA that favour polynya growth supports the likelihood of lower SLP over AABW formation regions during that time.

Online content

Any methods, additional references, Nature Portfolio reporting summaries, source data, extended data, supplementary information, acknowledgements, peer review information; details of author contributions and competing interests; and statements of data and code availability are available at <https://doi.org/10.1038/s41561-023-01368-z>.

References

- Stanley, R. H. R., Jenkins, W. J., Lott, D. E. & Doney III, S. C. Noble gas constraints on air–sea gas exchange and bubble fluxes. *J. Geophys. Res. Oceans* <https://doi.org/10.1029/2009JC005396> (2009).
- Jenkins, W. J., Lott, D. E. III & Cahill, K. L. A determination of atmospheric helium, neon, argon, krypton, and xenon solubility concentrations in water and seawater. *Mar. Chem.* **211**, 94–107 (2019).
- Jahne, B., Heinz, G. & Dietrich, W. Measurement of the diffusion coefficients of sparingly soluble gases in water. *J. Geophys. Res.* **92**, 10767–10776 (1987).
- Hamme, R. C. & Severinghaus, J. P. Trace gas disequilibria during deep-water formation. *Deep Sea Res.* **54**, 939–950 (2007).
- Nicholson, D. P., Khatiwala, S. & Heimbach, P. Noble gas tracers of ventilation during deep-water formation in the Weddell Sea. In *IOP Conf. Series: Earth and Environmental Science* <https://doi.org/10.1088/1755-1315/35/1/012019> (2016).
- Kuhlbrodt, T. et al. On the driving processes of the Atlantic meridional overturning circulation. *Rev. Geophys.* <https://doi.org/10.1029/2004RG000166> (2007).
- Jenkins, W. J. et al. The deep distributions of helium isotopes, radiocarbon, and noble gases along the U.S. GEOTRACES East Pacific zonal transect (GP16). *Mar. Chem.* **201**, 167–182 (2018).
- Jenkins, W. J. et al. A North Pacific meridional section (U.S. GEOTRACES GP15) of helium isotopes and noble gases I: deep water distributions. *Global Biogeochem. Cycles* **37**, e2022GB007667 (2023).
- Holzer, M., DeVries, T. & de Lavergne, F. Diffusion controls the ventilation of a Pacific Shadow Zone above abyssal overturning. *Nat. Commun.* <https://doi.org/10.1038/s41467-41021-24648-x> (2021).
- Loose, B. & Jenkins, W. J. The five stable noble gases are sensitive and unambiguous tracers of glacial meltwater. *Geophys. Res. Lett.* **41**, 2835–2841 (2014).
- England, M. H. & Maier-Reimer, E. Using chemical tracers to assess ocean models. *Rev. Geophys.* **39**, 29–70 (2001).
- Gebbie, G. & Huybers, P. The mean age of ocean waters inferred from radiocarbon observations: sensitivity to surface sources and accounting for mixing histories. *J. Phys. Oceanogr.* **42**, 291–305 (2012).
- Gebbie, G. & Huybers, P. Total matrix intercomparison: a method for determining the geometry of water mass pathways. *J. Phys. Oceanogr.* **40**, 1710–1728 (2010).

14. Gordon A. L. in *Encyclopedia of Ocean Sciences*, 3rd edn, Vol. 6 (eds Cochran, J. K., Bokuniewicz, J. H. & Yager L. P.) 120–126 (Elsevier, 2019).
15. Ohshima, K. I., Nihashi, S. & Iwamoto, K. Global view of sea-ice production in polynyas and its linkage to dense/bottom water formation. *Geosci. Lett.* **3**, 13 (2016).
16. Maqueda, M. A. M., Willmott, A. J. & Biggs, N. R. T. Polynya dynamics: a review of observations and modeling. *Rev. Geophys.* **42**, RG1004 (2004).
17. Moore, G. W. K., Alverson, K. & Renfrew, I. A. A reconstruction of the air–sea interaction associated with the Weddell polynya. *J. Phys. Oceanogr.* **32**, 1685–1698 (2002).
18. Weijer, W. et al. Local atmospheric response to an open-ocean polynya in a high-resolution climate model. *J. Clim.* **30**, 1629–1641 (2017).
19. Abram, N. J. et al. Evolution of the Southern Annular Mode during the past millennium. *Nat. Clim. Change* **4**, 564–569 (2014).
20. Bertler, N. A. N., Mayewski, P. A. & Carter, L. Cold conditions in Antarctica during the Little Ice Age—implications for abrupt climate change mechanisms. *Earth Planet. Sci. Lett.* **308**, 41–51 (2011).

Publisher’s note Springer Nature remains neutral with regard to jurisdictional claims in published maps and institutional affiliations.

Open Access This article is licensed under a Creative Commons Attribution 4.0 International License, which permits use, sharing, adaptation, distribution and reproduction in any medium or format, as long as you give appropriate credit to the original author(s) and the source, provide a link to the Creative Commons license, and indicate if changes were made. The images or other third party material in this article are included in the article’s Creative Commons license, unless indicated otherwise in a credit line to the material. If material is not included in the article’s Creative Commons license and your intended use is not permitted by statutory regulation or exceeds the permitted use, you will need to obtain permission directly from the copyright holder. To view a copy of this license, visit <http://creativecommons.org/licenses/by/4.0/>.

© The Author(s) 2024

Methods

Sampling and measurement methods

Water samples were collected and analysed for helium isotope and noble gases using methods documented in papers referred to in the main text. The acquisition pressure (depth), temperature and salinity for each sample are determined using standard GO-SHIP protocols to an accuracy of 0.1 dbar, 0.001 °C and 0.002 practical salinity units, respectively, and the data available from the appropriate international data repositories^{21,22}.

Processes that can alter noble gas saturation anomalies

The four arrows in Fig. 1c–e represent processes that can affect noble gas saturation anomalies, namely, (1) changes in barometric pressure (red) that, due to Henry's law²³, affect all gases equally; (2) changes in air injection (green), caused by bubble dissolution near the sea that disproportionately enhances the less soluble gases²⁴; and (3) addition of glacial melt water¹⁰, where glacial bubbles are forced into solution as ice melts. The heavier gases appear to become less saturated because the latent heat of fusion lowers the water temperature²⁵. (4) A fourth process (black arrows) represents the change in saturation anomalies associated with a change in temperature after equilibration with the atmosphere. This last can occur due to thermal disequilibrium as water masses form, where rapid cooling and resultant densification causes convection of water away from the sea surface before gases can equilibrate (the negative-trending black arrows). It also can result from geothermal heating (positive-trending black arrows).

The bin-averaged saturation anomalies of all four noble gases (Fig. 1c–e, small black squares) are shown in Extended Data Fig. 1 as solid blue (for the southern bin) and red (for the northern bin) lines. The red dashed lines represent the saturation anomalies corrected for the documented effects of geothermal heating between the southern and northern deep Pacific, as determined by Joyce et al.²⁶. The effects are smallest for ΔNe and greatest for ΔXe due to their respective slopes of solubility dependence on temperature².

The observations and their uncertainties (dashed ellipses) overlap with the prediction of a pure barometric effect, which can adequately and most probably explain the saturation anomaly differences. Another process that can change saturation anomalies includes geothermal heating (the black arrow), which we have already accounted for, whose slope is given by the ratio of the temperature dependences of the individual gas solubilities. An increase in thermal disequilibrium during water mass formation will produce a change in precisely the opposite direction along this vector^{4,10}. It is conceivable that one could construct an alternate vector pathway to the observations by arbitrarily combining an increase in air injection (part way along the green vector) with a reduction in thermal disequilibrium (hence along the black vector) during water mass formation. However, we contend this is an unlikely scenario for the following reasons. AABW is formed when extremely strong, cold and dry katabatic winds descend off the Antarctic continent and push the rapidly forming sea ice away from the shore to create and maintain a polynya. Polynyas are active sites of bottom water formation^{14,27}. The dynamics of these features are dominated by extremely large ocean–atmosphere heat fluxes¹⁶ that inject buoyancy into the atmosphere, lowering SLP^{17,28} and, if the polynya is large enough, generate atmospheric mesoscale cyclonic flow¹⁸. On the ocean side, there is a large amount of sea-ice production^{29,30}, primarily in the form of frazil ice^{31,32}. Despite high wind speeds, the presence of frazil ice suppresses wave amplitude and steepness^{33,34}, which in turn suppress air injection. Noble gas measurements in the Terra Nova Bay polynya show a suppression of this mechanism³⁴. Even discounting this suppression, any past increase in these winds that would be required to explain the increase in air injection would also result in an increase in latent and sensible heat extraction in the polynya, thereby spurring more ice formation, rapid buoyancy-driven convection and greater (rather than lesser) degree of thermal disequilibrium.

One final candidate explanation for the past change is to assert that AABW inherits noble gas characteristics from its progenitor water masses, most specifically North Atlantic Deep Water (NADW), and that the changes have occurred elsewhere (namely, in the North Atlantic). Comparing the saturation anomalies between AABW seen in the southern part of our section with NADW (Extended Data Fig. 3) appears to indicate that the only difference between the two is an overlaid signature of glacial melt water addition³⁵ and suggests that AABW otherwise ‘inherits’ the NADW gas signature. However, the noble gas concentrations of AABW differ substantially from NADW, in large part due to the temperature difference of their origins. AABW is around 3 °C colder than NADW and has (for example) an Ar content 5% larger and Xe content -8% greater in southern AABW in our section than NADW (there is an even bigger difference in Weddell Sea Bottom Water^{10,36}). It is difficult to construct a thermal disequilibrium scenario whereby the ‘inherited’ Ar concentration is raised by 5% and the Xe concentration is raised by precisely 8% when the molecular diffusivity of Xe is less than half that of Ar (ref. 3). The only explanation for the similarity of the saturation anomalies (excluding the glacial melt water, GMW, addition) is that the processes occurring during water mass formation are broadly similar between AABW and NADW (exclusive of glacial melt water addition).

Model and inverse solution

Gebbie and Huybers¹³ developed a box inverse method called total matrix intercomparison (TMI) that uses the global distribution of conserved tracers to diagnose the pathways by which various water masses populate the abyssal ocean. This was subsequently extended to constrain the transit timescales for these water masses¹² using the distribution of radiocarbon. We here use these model calculations to define the distribution of arbitrarily defined epochs (listed in Extended Data Table 1) throughout the deep ocean. Using the same bounds (latitude and neutral density) applied for the noble gas averaging, we estimate the percentage of each vintage associated with the two regions (southern and northern) in the third and fourth columns of Extended Data Table 1. We then solve for the mean SLPa (column 5 of Extended Data Table 1) for the centre point of each epoch that would be required to generate the observed 2.8 mbar palaeo-barometric difference between the regions.

Ocean circulation links between temporal and spatial variability

Surface conditions are transported to some parts of the subsurface ocean faster than others, and therefore past temporal variability leads to spatial variability in any snapshot of the ocean. Even globally uniform changes at the surface will lead to subsurface gradients through this mechanism^{37,38}. We observe a noble gas difference between -35° N and -10° S along the meridional section at 152° W and below 3.5 km depth. This difference is attributed to an apparent $p_{\star} = 2.8 \pm 0.4$ mbar SLP difference during the formation of the waters, where p_{\star} is the SLP analogy with P_{\star} , the pre-formed phosphate³⁹. If these two locations have waters with sufficiently different ages, or elapsed time since their component water masses were last at the surface, the difference could be explained by the history of past surface changes.

Here we calculate the age distributions for representative abyssal North and South Pacific sites from an empirically derived steady-state ocean circulation model that fits modern-day climatological distributions of temperature, salinity, phosphate, nitrate, oxygen, oxygen–isotope ratio and radiocarbon¹². Both sites have waters with a wide range of ages from a few hundred to a few thousand years (Extended Data Figs. 3 and 4) because of the many routes from abyssal water formation sites and the substantial time for mixing to occur⁴⁰. The age distributions are peaked at about 800 and 1,000 years for the South and North Pacific sites, respectively, indicating that the South Pacific has waters of a younger age due to being closer to Antarctic sites of abyssal water formation. Although abyssal Pacific waters move slowly and remain in

the basin for a long time, there are clear meridional differences in the ages of seawater. Note that there is an expected difference between the modal (peak) and mean ages seen in Extended Data Fig. 4.

The pre-formed pressure value today (that is, 2023 CE) at the North Pacific sample location r_{sp} is related to the past via a convolution equation,

$$p_{\star}(2023 \text{ CE}, r_{np}) = \sum_{i=1}^{4,000} g_i(r_{np}) p_{\star}(2023 \text{ CE} - i, r_b), \quad (2)$$

which is a sum of contributions from g_i , the annually resolved age distribution, operating on the past surface boundary conditions at r_b , the source location of the i th water mass component⁴¹. The distribution is denoted g_i to recall the discrete time Green's function and is available from the steady-state circulation for the past 4,000 years. The sum of g_i values is greater than 0.99, indicating that 4,000 years is sufficient to capture over 99% of the age distribution. Note that g_i is dimensionless and has been translated into a mass fraction per year to be displayed in continuous, rather than discrete, form in Extended Data Fig. 4. A similar equation is available for the South Pacific location. The difference between the North and South Pacific age distributions is key for mapping time variability into space.

The difference between equation (2) and an equivalent South Pacific equation yields a constraint on the pre-formed pressure difference:

$$\Delta p_{\star}(2023 \text{ CE}, r_{np}, r_{sp}) = \sum_{i=1}^{4,000} \Delta g_i p_{\star}(2023 \text{ CE} - i, r_b), \quad (3)$$

where Δp_{\star} is the north minus south pre-formed pressure difference and the new Green's function is a difference (that is, $\Delta g_i = g_i(r_{np}) - g_i(r_{sp})$) where r_{sp} refers to the South Pacific location. This equation is simplified under the assumption that the Green's functions are unchanging in time, an assumption that appears to be true to first order given the slight modifications to ocean hydrographic structure over the past 150 years¹². It is also assumed that past changes in pre-formed pressure are globally uniform, which is clearly untrue and will be interpreted later in this document. In concept, equation (3) relates a spatial gradient on the left-hand side to a surface timeseries on the right-hand side.

The north–south difference in age distributions show negative values around 500 years and positive values around 1,500 years (green line, Extended Data Fig. 4), which is possible because differences of distributions are no longer required to be non-negative. If surface conditions imprinted the signal of higher pressure 500 years ago, it would be reflected with South Pacific pre-formed pressure being higher than the North Pacific. What is actually observed is the North Pacific being higher than the South, suggesting that surface conditions had lower pressure 500 years ago. Any timeseries of surface changes that projects on Δg_i , however, also affects the observed meridional gradient in p_{\star} , and a quantitative method is required to sort through the range of plausible solutions.

Another concern is whether ocean mixing would erase the signal of past surface conditions before they could be observed today. The magnitude and shape of the curve that represents Δg_i in Extended Data Fig. 4 contain information about this mixing and damping of surface signals through time. In some sense, Δg_i is analogous to an ocean circulation filter that acts to transform the surface timeseries. Thus, any quantitative method must be able to perform a deconvolution to determine whether north–south age differences are large enough to explain the observed pre-formed pressure spatial gradient.

Seawater vintages

It is highly unlikely that a noble gas record retains information about year-to-year to even decade-to-decade changes. Therefore, we simplify the analysis by defining vintages of seawater that describe the epoch

during which water was last at the surface. Vintages have previously been used to describe the year that waters left the surface⁴², like a vintner describes a batch of wine, and here we use the term for a much wider range of years. Here we define the following vintages: MOD (1800–2022 CE), LIA (1300–1800 CE), MCA (800–1300 CE), DACP (300–800 CE), RWP (200 BCE to 300 CE) and the pre-RWP (before 200 BCE). Note that these time intervals do not strictly match definitions in the literature⁴³, but instead are chosen to prioritize 500-year intervals for ease of later interpretation. Note that the pre-RWP and MOD vintages are respectively larger and smaller than 500 years. Thus, the apparent abundance comparability between pre-RWP and RWP along the section (Fig. 2a) arises due to this discrepancy.

The description of the waters that bathe the North and South Pacific sites can now be simplified to the combination of these six vintages. The mass fraction of each vintage is calculated by integrating the age distribution over the appropriate time interval, for example, for the LIA,

$$m_{LIA}(r_{np}) = \sum_{i=2023-1800}^{2023-1300} g_i(r_{np}), \quad (4)$$

where m_{LIA} is the mass fraction of LIA water and the time indices account for the time elapsed between the LIA and today. Following the development above, the key relationship between temporal and spatial gradients is simplified to

$$\Delta p_{\star}(2023 \text{ CE}, r_{np}, r_{sp}) = \sum_{j=1}^6 \Delta m_j p_{\star}(j, r_b), \quad (5)$$

where the summation includes six vintages, the mass-fraction difference is $\Delta m_j = m_j(r_{np}) - m_j(r_{sp})$, and the history of surface boundary conditions is identified with a particular climate epoch. This simplification makes a trade-off: it will be more difficult to explain the observations, but all solutions will represent a realistic system with centennial-scale changes in climate.

Inverse problem

Equation (5) represents an underdetermined problem with one constraint, six unknowns and infinitely many solutions. Here we provide information regarding the expected covariance of the solution to construct a statistical solution with its uncertainty. The solution method, detailed next, is based on the Gauss–Markov theorem⁴⁴.

For ease of notation, we collate the unknown parameters and the vintage mass fractions into vectors:

$$\mathbf{x} = \begin{pmatrix} p_{\star}(\text{MOD}, r_b) \\ p_{\star}(\text{LIA}, r_b) \\ p_{\star}(\text{MCA}, r_b) \\ p_{\star}(\text{DACP}, r_b) \\ p_{\star}(\text{RWP}, r_b) \\ p_{\star}(\text{preRWP}, r_b) \end{pmatrix}, \quad (6)$$

and

$$\mathbf{m} = \begin{pmatrix} \Delta m_{\text{MOD}} \\ \Delta m_{\text{LIA}} \\ \Delta m_{\text{MCA}} \\ \Delta m_{\text{DACP}} \\ \Delta m_{\text{RWP}} \\ \Delta m_{\text{preRWP}} \end{pmatrix}. \quad (7)$$

Now the constraint is symbolically described as

$$y = \mathbf{m}^T \mathbf{x} + \mathbf{n}, \tag{8}$$

where the observation is $y = \Delta p_*(2023 \text{ CE}, r_{\text{np}}, r_{\text{sp}})$, T is the vector transpose, and \mathbf{n} is a reminder that the observational fit is not expected to be perfect.

The Gauss–Markov theorem provides a means to solve an under-determined problem via the solution formula

$$\tilde{\mathbf{x}} = \mathbf{C}_{\text{xx}} \mathbf{m} (\mathbf{m}^T \mathbf{C}_{\text{xx}} \mathbf{m} + \mathbf{C}_{\text{nn}})^{-1} y, \tag{9}$$

which is valid so long as the quantity in parentheses is invertible. We denote $\tilde{\mathbf{x}}$ with a tilde to mark that it is a solution. The observation y is not bold because it is a scalar, not a vector. This solution satisfies a number of advantageous statistical properties, such as being unbiased and minimizing the uncertainty of each solution element. Such properties only hold in the case that the input statistical information, the solution and observation covariance matrices \mathbf{C}_{xx} and \mathbf{C}_{m} are valid.

The observational covariance is easily set as it is the observational variance: $\mathbf{C}_{\text{nn}} = (0.4 \text{ mbar})^2$. The solution covariance has two components: (1) setting the baseline or reference for the pre-formed pressure anomalies and (2) a description of the expected climate variability. Here we define the reference for the anomalies to be the pre-industrial (all vintages but MOD) p_* average. Such a constraint could be added to the system as a second observational equation of the following form:

$$\overline{p_*} = \sum_{j=2}^6 \frac{1}{5} p_*(j, r_b) = \mathbf{m}^T \mathbf{x} = 0, \tag{10}$$

where $1/5$ arises from the average over five vintages. Instead we recognize that this constraint imposes a covariance of the form, $\mathbf{C}_{\text{xx}} = \sigma^2 \mathbf{m}^T \mathbf{m}$ where σ is the expected deviation from a perfect zero reference level. Here we choose the small but non-zero value of $\sigma = 10^{-4}$ mbar.

For part 2 of the solution covariance, we experiment with three cases with increasing complexity.

Minimum variance solution. We define the solution covariance to conservatively assume that p_* has a standard deviation of 10 mbar based upon existing SLP gradients and historical model simulations⁴⁵. All epochs are assumed to vary independently. The solution covariance is

$$\mathbf{C}_{\text{xx}} = \begin{pmatrix} 100.0 & 0.0 & 0.0 & 0.0 & 0.0 & 0.0 \\ 0.0 & 100.0 & 0.0 & 0.0 & 0.0 & 0.0 \\ 0.0 & 0.0 & 100.0 & 0.0 & 0.0 & 0.0 \\ 0.0 & 0.0 & 0.0 & 100.0 & 0.0 & 0.0 \\ 0.0 & 0.0 & 0.0 & 0.0 & 100.0 & 0.0 \\ 0.0 & 0.0 & 0.0 & 0.0 & 0.0 & 100.0 \end{pmatrix} \text{mbar}^2. \tag{11}$$

The solution covariance from equation (2) that defines the anomaly reference level is added to this matrix, as is done in all cases to follow.

Minimum trend. The climate epochs are several hundred years long, but the climate is known to have variability at these scales and longer. In this second case, we define the solution covariance such that trends have an expected magnitude no larger than $p' = 4$ mbar per century based upon the few long timescale climate frequency spectra that are available⁴⁶. We define a matrix D that calculates differences between all combinations of vintages, and where the expected output for vintages i and j is as follows:

$$\Delta p_*(i, j) = p' \Delta t(i, j), \tag{12}$$

where $\Delta t(i, j)$ is the time difference between the midpoints of vintages i and j . The resulting covariance matrix is DD^T where each element is scaled by $(1/\Delta p_*(i, j))^2$.

Combined covariance matrix. The combined covariance matrix (labelled ‘min-trend-variance’) is a sum of the covariance from (1) the definition of the reference level for pre-formed pressure anomalies, (2) the expected variance of pre-formed pressure about this reference level (‘min-variance’) and (3) the expectation of correlation between vintages that are adjacent in time (‘min-trend’).

Inverse solutions

The three inverse solutions use a variety of statistical input from different information sources but converge to a common solution between 1,500 and 500 years ago (Extended Data Fig. 3). This time period is marked by a statistically substantial ($P = 0.05$) inferred decrease of SLP by 14 ± 10 mbar over time. The solutions also have common elements before 1,500 years ago. The greatest differences come in relation to LIA to modern changes. Because seawater in the abyssal North Pacific has very little modern vintage water, we are unable to conclusively place modern SLP in context of previous changes. It is possible that modern SLP is about the same as the LIA, or it could be as much as 15 mbar higher. Thus, the contrast is between LIA and older epochs.

The problem formulation has proceeded by assuming that SLP changes are globally uniform, but such large changes in SLP would indicate a change in the mass of the atmosphere. The low solubility of nitrogen and oxygen in seawater make such large mass changes unlikely. Instead, the results of the inverse solution should be interpreted in a more nuanced way. Signals in abyssal waters primarily reflect surface signals at the sites of formation in polar oceans, and we lack direct information about the tropics and subtropics here. Thus, inferred changes in the LIA and earlier should be interpreted as changes in polar oceans, and constraints on the global mass of the atmosphere can be balanced by opposing changes in the tropics.

It is still debated whether the LIA is a North Atlantic-centric or global phenomenon, although recent evidence points to a parallel Antarctic effect during the LIA^{20,47,48}. Our inferences of SLP change are best interpreted as changes in polar regions and cannot directly be pinpointed as Northern or Southern Hemisphere variability. Due to the fact that the water mass composition of the abyssal Pacific is dominated by southern source waters, however, we suggest that the noble gas signal is more easily explained by changes in and around Antarctica. North Atlantic waters occupy less than half the mass of Antarctic waters in the abyssal North Pacific⁴⁹ and would require an unrealistically large SLP signal that is more than twice as large (30+ mbar) if the Antarctic region did not participate in the LIA.

SLP differences between climate eras

The scenario with the highest degree of sophistication is labelled ‘min-trend-variance’. The long-term trend between the LIA and the earliest climate eras (DACP, RWP and pre-RWP) is substantial at the 95% confidence level (Extended Data Table 2). In particular, we estimate that the pre-RWP to LIA decrease of 19 ± 11 mbar (2σ error bars) is well constrained by the data. Differences over shorter time periods are generally not substantial. It is also difficult to find a substantial relation to modern SLPs.

Limitations of the model used

It should be noted that the reference level for the SLPa is constrained by the representation of the individual vintages in the bottom water mixture of our observations. Since the modern vintage remains poorly represented, the reference point is effectively the average SLP of the remaining five better represented vintages. That is, the curves presented in Fig. 2b and Extended Data Fig. 3 are only loosely tethered to modern values. Put another way, our observations only constrain the

overall SLP contrast between the RWP/PRWP and LIA periods. One could, in principle, arbitrarily shift the reference level such that the curve intersects zero in the MOD, but the corresponding error bars would be negatively impacted.

The reader should be wary of the fact that the model used to obtain the chronology and extent of attenuation by mixing is by nature a steady-state model. Past changes in the intensity of the circumpolar trough will lead to alteration of the strength of the Southern Hemisphere westerlies. Changes in the strength of the Southern Hemisphere westerlies could have implications for the strength of the Atlantic deep overturning cell, formation rates of Antarctic Intermediate Water, the recycling of NADW to the surface and even the quantity of NADW that fills the deep Pacific. A major complication is that the age of seawater for the abyssal ocean is primarily determined by observations of radiocarbon¹², which is itself an age tracer that reflects the integrated effect of thousands of years of possibly varying circulation due to its long half-life. The few decades of background radiocarbon observations that were used for the 2012 TMI inversion¹² (used in this work) are not sufficient to determine whether today's radiocarbon observations are in equilibrium with today's circulation. It is probably more likely that the present-day oceanic radiocarbon distribution represents a complicated average of the circulation over the past 3,000–4,000 years. Seen in this light, the circulation used in this work is close to an average estimate of circulation over the Common Era and thus a reasonable starting point for interpreting the noble gas data.

Even if the oceanic age distribution used here is a good Common Era average, the effect of circulation variability on the ocean's mean age is still not captured. The response of the oceanic age distribution is complex, but consider the case where oceanic circulation rates (both advective and diffusive) are 30% stronger. The time required for the change in physical circulation to be reflected in an abyssal tracer, such as age, can be shown to be roughly equal to the abyssal age itself. For waters that are diagnosed to be of the LIA vintage, they are about 400 years old on average. We expect the age of this water to decrease to about 300 years over a 300-year time period. With the 500-year time intervals used for pre-industrial climate epochs, we would still diagnose these waters as being from the LIA.

In summary, the effect of circulation variability makes the accurate inference of earlier climate epochs more difficult. If age distributions could shift by 30%, then waters of the RWP could have an age error approaching 600 years. With 500-year climate epochs, we start to encounter the case where a small percentage of RWP waters are actually from the pre-RWP or the DACP. This affects not only the 'true mean age' but also the degree of attenuation by mixing.

Data availability

The noble gas data have been archived at the US BCO-DMO (Biological and Chemical Oceanography Data Management Office)^{50,51}. The Ne data^{52,53} are available under two references: <https://doi.org/10.26008/1912/bco-dmo.862182.1> and <https://doi.org/10.26008/1912/bco-dmo.862220.1>, and the Ar, Kr and Xe data under <https://doi.org/10.26008/1912/bco-dmo.877873.1> and <https://doi.org/10.26008/1912/bco-dmo.877899.1>. The hydrographic (pressure, temperature and salinity) data are available with DOI references <https://doi.org/10.26008/1912/bco-dmo.777951.6> and <https://doi.org/10.26008/1912/bco-dmo.824867.5>, respectively.

Code availability

The code, along with algorithms, relevant figures and other documentation, is archived on Zenodo at <https://doi.org/10.5281/zenodo.10368927>.

References

- Casciotti, K., Cutter, G. A. & Lam, P. J. Bottle file from Leg 1 (Seattle, WA to Hilo, HI) of the US GEOTRACES Pacific Meridional Transect (PMT) cruise (GP15, RR1814) on R/V Roger Revelle from September to October 2018. *Biological and Chemical Oceanography Data Management Office* <https://doi.org/10.26008/1912/bco-dmo.777951.6> (2021).
- Casciotti, K., Cutter, G. A. & Lam, P. J. Bottle file from Leg 2 (Hilo, HI to Papeete, French Polynesia) of the US GEOTRACES Pacific Meridional Transect (PMT) cruise (GP15, RR1815) on R/V Roger Revelle from October to November 2018. *Biological and Chemical Oceanography Data Management Office* <https://doi.org/10.26008/1912/bco-dmo.824867.5> (2021).
- Henry, W. Experiments on the quantity of gases adsorbed by water, at different temperatures, and under different pressures. *Philos. Trans. R. Soc.* **93**, 29–42, 274–276 (1803).
- Jenkins, W. J. The use of anthropogenic tritium and ³He to study subtropical gyre ventilation and circulation. *Philos. Trans. R. Soc.* **A325**, 43–61 (1988).
- Gade, H. G. When ice melts in sea water: a review. *Atmos. Ocean* **31**, 139–165 (1993).
- Joyce, T. M., Warren, B. A. & Talley, L. D. The geothermal heating of the abyssal sub-Arctic Pacific Ocean. *Deep Sea Res. Part A* **33**, 1003–1015 (1986).
- Gordon, A. L. Southern Ocean polynya. *Nat. Clim. Change* **4**, 249–250 (2014).
- Wenta, M. & Cassano, J. J. The atmospheric boundary layer and surface conditions during katabatic wind events over the Terra Nova Bay polynya. *Remote Sens.* **12**, 4160 (2020).
- Ackley, S. F., Smith, M. M., Guest, P., Herman, A. & Hayley, S. Winds, waves and ice formation in a coastal polynya. In *26th IAHR International Symposium on Ice, ID No. 22118* (IAHR, 2022).
- Ackley, S. F. et al. Sea-ice production and air/ice/ocean/biogeochemistry interactions in the Ross Sea during the PIPERS 2017 autumn field campaign. *Ann. Glaciol.* **61**, 181–195 (2020).
- Ito, M. et al. Observations of supercooled water and frazil ice formation in an Arctic coastal polynya from moorings and satellite imagery. *Ann. Glaciol.* **56**, 307–314 (2015).
- Nakata, K., Ohshima, K. I. & Nishihashi, S. Mapping of active frazil for antarctic coastal polynyas, with an estimation of sea-ice production. *Geophys. Res. Lett.* **48**, e2020GL091353 (2021).
- Feltham, D. L., Untersteiner, N., Wettlaufer, J. S. & Worster, M. G. Sea ice is a mushy layer. *Geophys. Res. Lett.* **33**, L14501 (2006).
- Loose, B., Stammerjohn, S., Sedwick, P. & Ackley, S. Sea ice formation, glacial melt and the solubility pump boundary conditions in the Ross Sea. *J. Geophys. Res. Oceans* <https://doi.org/10.1029/2022JC019322> (2023).
- Jenkins, W. J. et al. A North Pacific Meridional Section (U.S. GEOTRACES GP15) of helium isotopes and noble gases II: shallow distributions and tritium. *Global Biogeochem. Cycles* **37**, e2022GB007667 (2023).
- Loose, B. et al. Estimating the recharge properties of the deep ocean using noble gases and helium isotopes. *J. Geophys. Res. Oceans* **121**, 5959–5979 (2016).
- Gebbie, G. & Huybers, P. The Little Ice Age and 20th-century deep Pacific cooling. *Science* **363**, 70–74 (2019).
- Scheen, J. & Stocker, T. F. Effect of changing ocean circulation on deep ocean temperature in the last millennium. *Earth Syst. Dynam.* **11**, 925–951 (2020).
- The international thermodynamic equation of seawater—2010: calculation and use of thermodynamic properties. *Intergovernmental Oceanographic Commission* <http://www.TEOS-10.org> (2010).
- Khatiwal, S., Visbeck, M. & Schlosser, P. Age tracers in an ocean GCM. *Deep Sea Res.* **48**, 1423–1441 (2001).
- Hall, T. M. & Haine, T. W. N. On ocean transport diagnostics: the idealized age tracer and the age spectrum. *J. Phys. Oceanogr.* **32**, 1987–1991 (2002).

42. Pickart, R. S., Torres, D. J. & Clarke, R. A. Hydrography of the Labrador Sea during active convection. *J. Phys. Oceanogr.* **32**, 428–457 (2002).
43. Paasche, O. & Bakke, J. Defining the Little Ice Age. *Clim. Past Discuss.* **5**, 2159–2175 (2010).
44. Wunsch C. *Discrete Inverse and State Estimation Problems. With Geophysical Fluid Applications* (Cambridge Univ. Press, 2006).
45. Hakim, G. J. et al. The last millennium climate reanalysis project: framework and first results. *J. Geophys. Res. Atmos.* **121**, 6745–6764 (2016).
46. Huybers, P. & Curry, W. Links between annual, Milankovitch and continuum temperature variability. *Nature* **441**, 329–332 (2006).
47. Rhodes, R. H. et al. Little Ice Age climate and oceanic conditions of the Ross Sea, Antarctica from a coastal ice core record. *Clim. Past* **8**, 1223–1238 (2012).
48. Simms, A. R., et al. Evidence for a ‘Little Ice Age’ glacial advance within the Antarctic Peninsula—examples from glacially-overrun raised beaches. *Quat. Sci. Rev.* **271** (2021).
49. Johnson, G. C. Quantifying Antarctic bottom water and North Atlantic deep water volumes. *J. Geophys. Res. Oceans* <https://doi.org/10.1029/2007JC004477> (2008).
50. Jenkins, W. J., German, C. R. & Lott, D. E. I. Concentrations of dissolved argon, krypton, and xenon from Niskin bottle samples collected on Leg 1 (Seattle, WA to Hilo, HI) of the US GEOTRACES Pacific Meridional Transect (PMT) cruise (GP15, RR1814) on R/V Roger Revelle from Sept–Oct 2018. *Biological and Chemical Oceanography Data Management Office* <https://doi.org/10.26008/1912/bco-dmo.877873.1> (2022).
51. Jenkins, W. J., German, C. R. & Lott, D. E. I. Concentrations of dissolved argon, krypton, and xenon from Niskin bottle samples collected on Leg 2 (Hilo, HI to Papeete, French Polynesia) of the US GEOTRACES Pacific Meridional Transect (PMT) cruise (GP15, RR1815) on R/V Roger Revelle from Oct–Nov 2018. *Biological and Chemical Oceanography Data Management Office* <https://doi.org/10.26008/1912/bco-dmo.877899.1> (2022).
52. Jenkins, W. J. & German, C. R. Helium isotope with helium and neon concentration data from Leg 1 (Seattle, WA to Hilo, HI) of the US GEOTRACES Pacific Meridional Transect (PMT) cruise (GP15, RR1814) on R/V Roger Revelle from September to October 2018. *Biological and Chemical Oceanography Data Management Office* <https://doi.org/10.26008/21912/bco-dmo.862182.862181> (2021).
53. Jenkins W. J. & German C. R. Helium isotope with helium and neon concentration data from Leg 2 (Hilo, HI to Papeete, French Polynesia) of the US GEOTRACES Pacific Meridional Transect (PMT) cruise (GP15, RR1815) on R/V Roger Revelle from Oct–Nov 2018. *Biological and Chemical Oceanography Data Management Office* <https://doi.org/10.26008/21912/bco-dmo.862220.862221> (2021).

Acknowledgements

We are grateful to the chief scientists, seagoing technicians and marine crew who made the GEOTRACES GP15 Pacific Meridional Transect such a success, plus the GEOTRACES organizing committee that made the programme possible (especially B. Anderson). The analytical work as well as interpretation by W.J.J. and C.R.G. was supported by the US National Science Foundation grant number OCE-1756138. A.M.S. was supported under NSF grant OCE-2122427, and G.G. was funded by NSF grant OCE-83192900. Such high-quality measurements would not be possible without the labour and expertise of D. E. Lott III and K. Cahill. We also thank K. Hughen and A. Gordon for helpful discussions.

Author contributions

W.J.J. made the noble gas measurements, wrote the framework of the manuscript, did some of the statistical analysis, prepared most of the figures and identified importance of the polynya linkage to SLP. A.M.S. contributed to the interpretation, writing and many aspects of the palaeo-oceanographic linkages. G.G. developed and applied the inverse model calculations used to compute the size of the SLPa, and the statistics associated with it, required to explain the observations. He also contributed to interpretation and the writing of the manuscript. C.R.G. was involved in obtaining funding for the research and contributed to both interpretation and writing of the manuscript.

Competing interests

The authors declare no competing interests.

Additional information

Extended data is available for this paper at <https://doi.org/10.1038/s41561-023-01368-z>.

Supplementary information The online version contains supplementary material available at <https://doi.org/10.1038/s41561-023-01368-z>.

Correspondence and requests for materials should be addressed to W. J. Jenkins.

Peer review information *Nature Geoscience* thanks the anonymous reviewers for their contribution to the peer review of this work. Primary Handling Editor: James Super, in collaboration with the *Nature Geoscience* team.

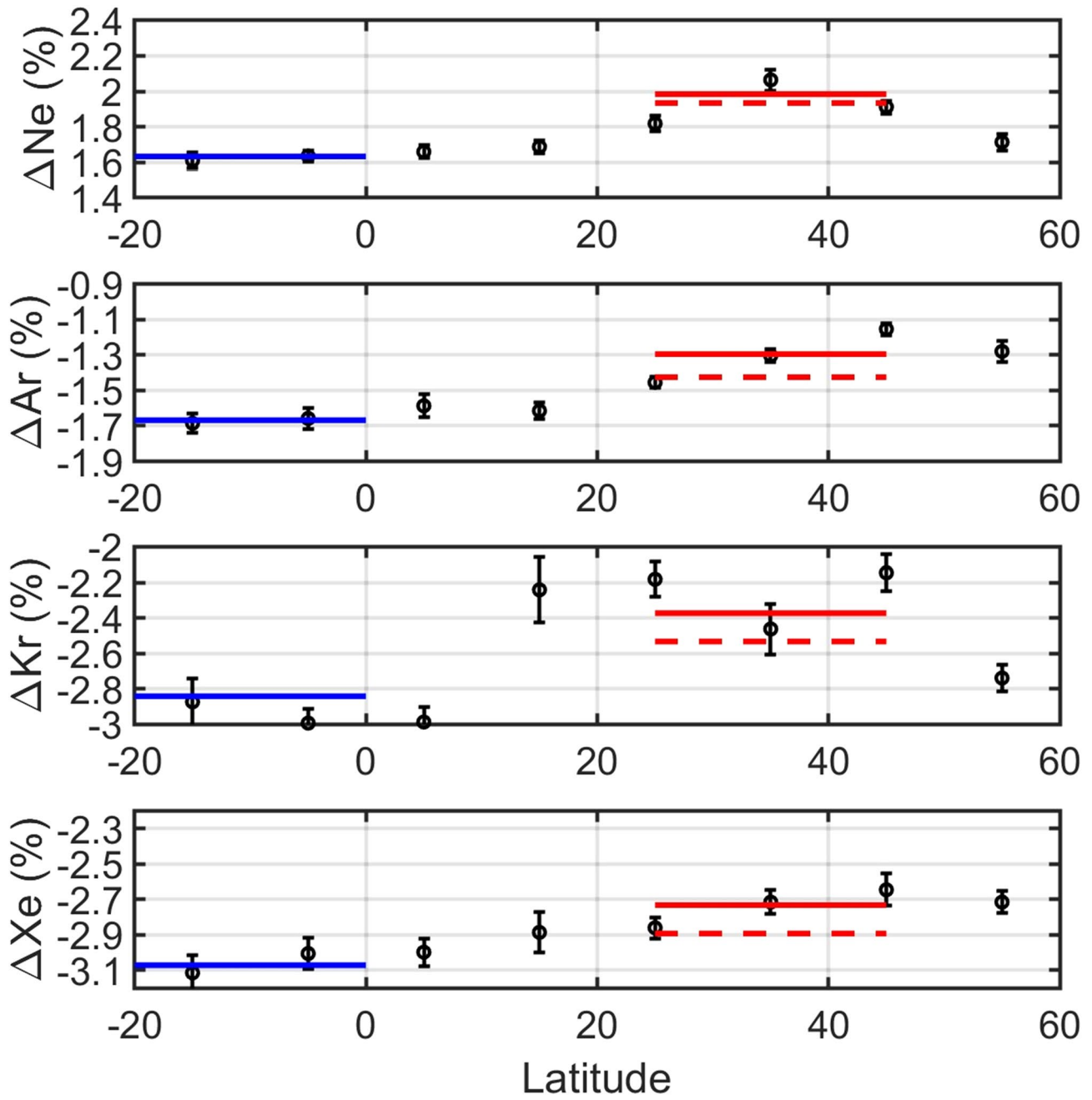
Reprints and permissions information is available at www.nature.com/reprints.

Extended Data Table 1 | Vintage mixtures for the two regions. The acronyms correspond to as follows: MOD Modern Era, LIA Little Ice Age, MCA Medieval Climate Anomaly, DACP Dark Ages Cold Period, RWP Roman Warm Period, and PRE-RWP Pre-Roman Warm Period

Vintage Epoch	Year Range	Southern Region	Northern Region	SLP Anomaly	σ_{SLP}
	years	%	%	mbar	mbar
MOD	> 1800 CE	3.1	1.8	-5.7	6.6
LIA	1300 – 1800 CE	28.1	16	-10.8	3.3
MCA	800 – 1300 CE	30.8	27	-4.9	5.2
DACP	300 – 800 CE	19.3	23.9	2.6	5.4
RWP	200 BCE – 300 CE	10.0	15.3	5.3	5.2
PRE-RWP	<200 BCE	8.7	16	7.8	5.5

Extended Data Table 2 | Sea-level pressure differences in millibars between climate eras, as defined by the difference of the value during one vintage (rows) and another vintage (columns) calculated in the min-trend-variance case. Some differences are significant at the 67% (bold) and 95% (bold, red) confidence levels. The vintages are: modern (MOD, 1800 - 2022 CE), Little Ice Age (LIA, 1300- 1800 CE), Medieval Climate Anomaly (MCA, 800 - 1300), Dark Ages Cold Period (DACP, 300 -800 CE), Roman Warm Period (RWP, 200 BCE - 300 CE), and the pre-Roman Warm Period (preRWP, before 200 BCE)

Vintage	MOD	LIA	MCA	DACP	RWP	Pre-RWP
MOD	0.0±0.0	5.1±7.2	-0.78±8.9	-8.3±8.6	-10.9±8.3	-13.5±8.2
LIA	-5.1±7.2	0.0±0.0	-5.8±7.9	-13.4±6.7	-16.0±6.1	-18.5±5.6
MCA	0.8±8.9	5.8±7.9	0.0±0.0	-7.5±7.8	-10.2±8.1	-12.7±8.3
DACP	8.3±8.6	13.4±6.7	7.5±7.8	0.0±0.0	-2.6±8.5	-5.1±9.5
RWP	10.9±8.3	16.0±6.1	10.2±8.1	2.6±8.5	0.0±0.0	-2.5±9.0
pre-RWP	13.5±8.2	18.5±5.6	12.7±8.3	5.1±9.5	2.5±9.0	0.0±0.0

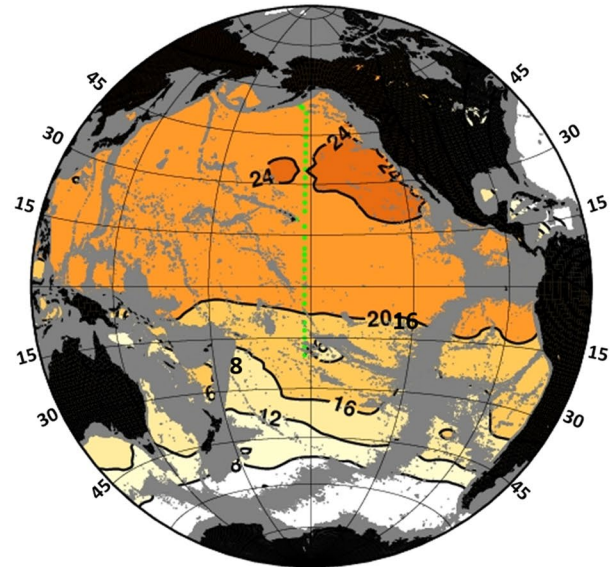
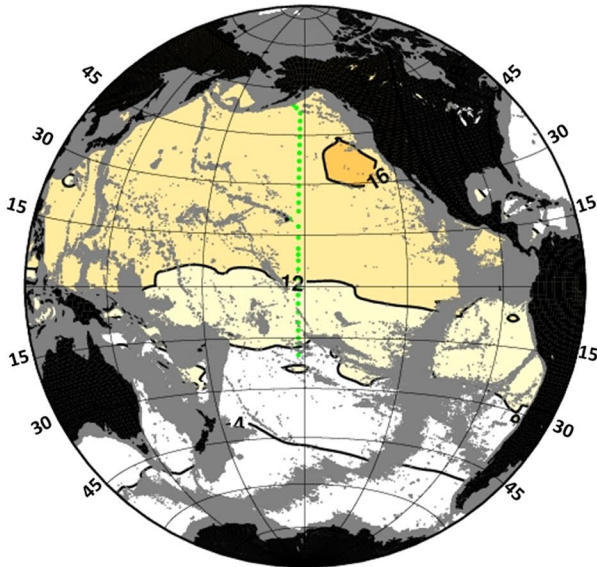


Extended Data Fig. 1 | Binned averages over 10° latitude of bottom water (> 3400 m depth) noble gas saturation anomalies. Binned averages over 10° latitude of bottom water (> 3400 m depth) noble gas saturation anomalies for the section. The error bars are the standard error of the mean and the number of points involved in each of the eight ten-degree binned averages are (from south to north) are from 18, 17, 20, 12, 12, 13, 13 and 18 measurements respectively. The

solid blue horizontal lines are the averages of all bottom water samples taken in the range of 20°S to the equator (not an average of the binned averages) and similarly for the solid red horizontal lines for 25–45°N. The horizontal red dashed lines are the northern averages corrected for the effects of geothermal heating (see text).

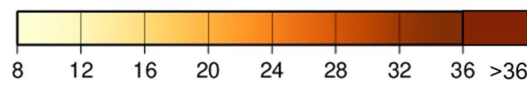
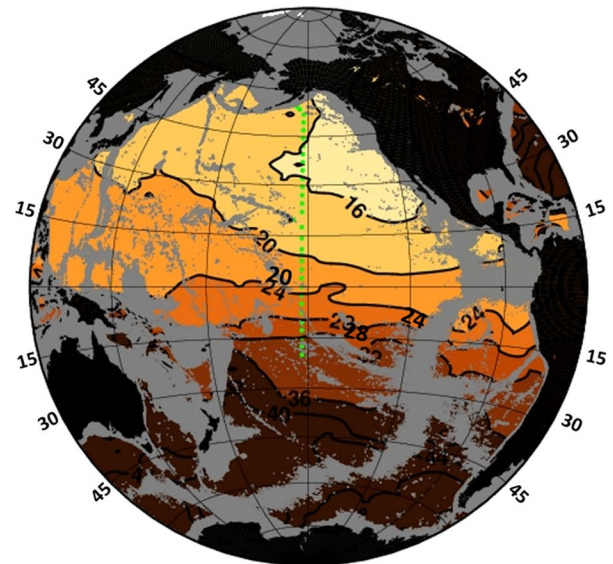
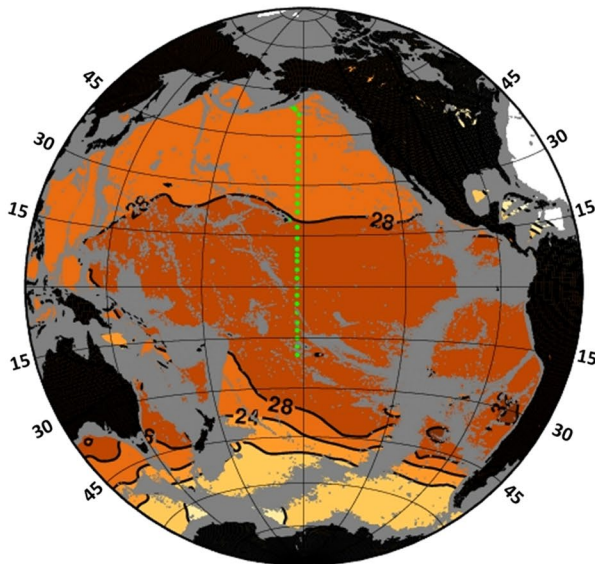
a) Roman Warm Period (200 BCE – 300 CE)

b) Dark Ages Cold Period (300 – 800 CE)



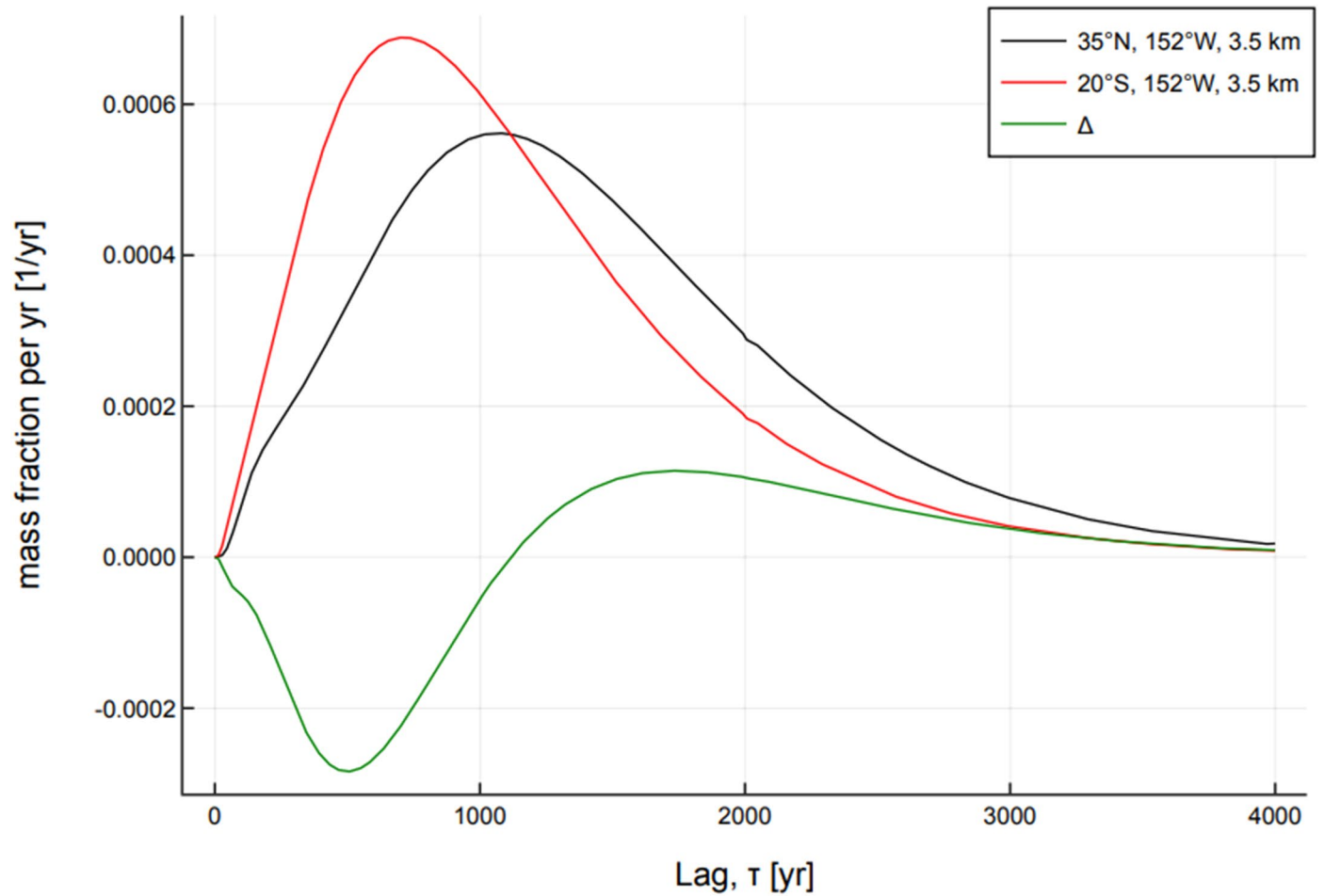
c) Medieval Climate Anomaly (800 – 1300 CE)

d) Little Ice Age (1300 – 1800 CE)



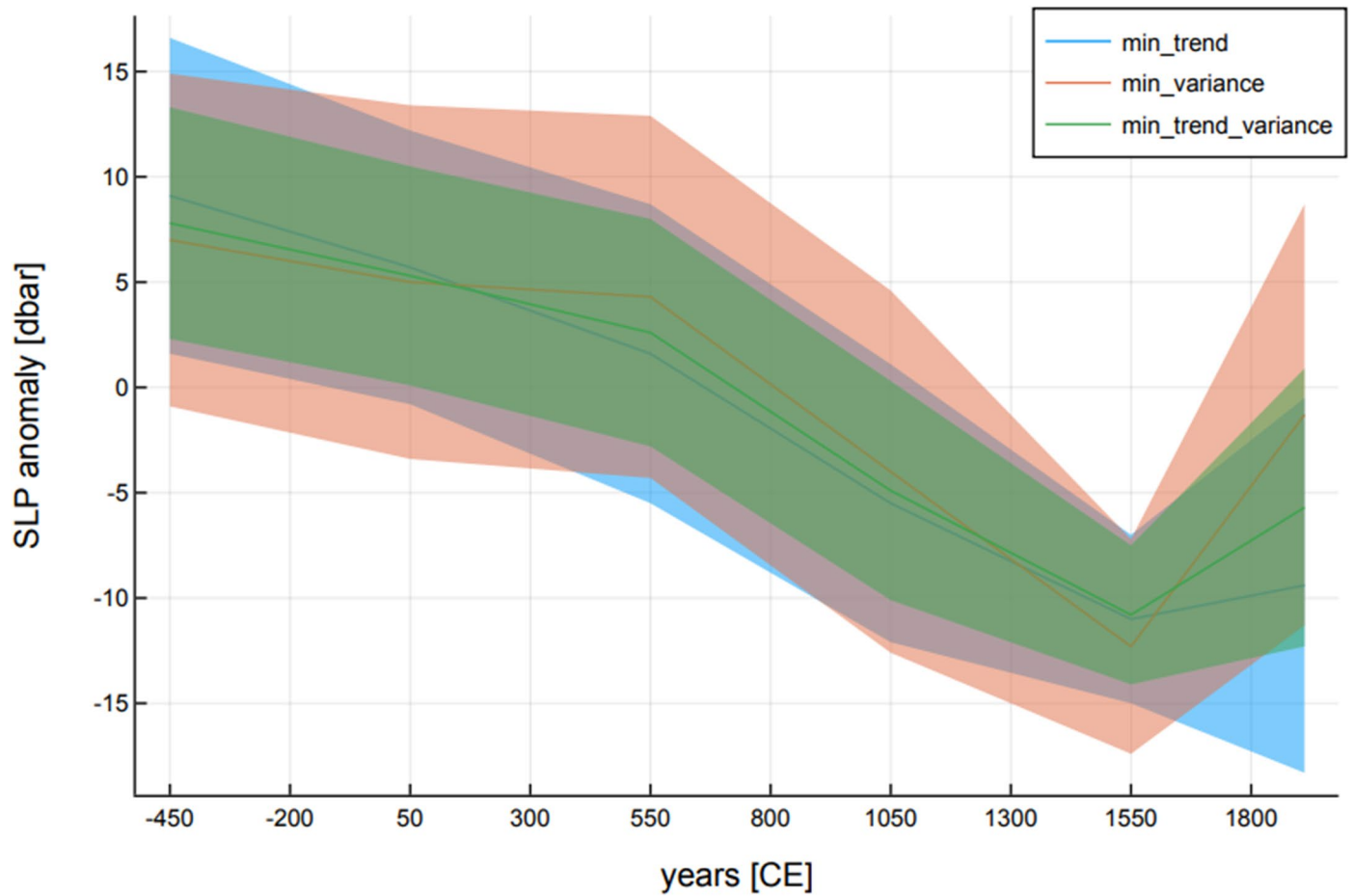
Vintage (%) at 3500m

Extended Data Fig. 2 | Maps of the percentage contribution of four of the vintages at 3500 m in the Pacific.



Extended Data Fig. 3 | 'Continuum' age distributions from the North and South Pacific along 152°W and 3.5 km depth. 'Continuum' age distributions from the North (black) and South (red) Pacific along 152°W and 3.5 km depth, as well as the north minus south difference (green), as calculated from an

empirically-derived ocean circulation model. The integral under the black and red curves is such that the total mass fraction is unity. Lags on the x-axis refer to the time lag of subsurface signals relative to the surface.



Extended Data Fig. 4 | Inferred historical sea level pressure variations. All results use the identical noble gas observational information, but differ in the assumed solution covariance matrix (blue: min-trend, red: min-variance, green: min-trend-variance). Error ribbons represent the 1σ uncertainty level. Results from each vintage are plotted as a single value at the midpoint of the interval.